Journal of Power Sources 196 (2011) 4911–4922

Contents lists available at ScienceDirect

Journal of Power Sources

journal homepage: www.elsevier.com/locate/jpowsour

# Electrochemical, structural and surface characterization of nickel/zirconia solid oxide fuel cell anodes in coal gas containing antimony

Olga A. Marina[a,*], Larry R. Pederson[b], Christopher A. Coyle[a], Edwin C. Thomsen[a], Ponnusamy Nachimuthu[a], Danny J. Edwards[a]

[a] Pacific Northwest National Laboratory, Richland, WA 99352, USA
[b] Center for Nanoscale Science and Engineering, North Dakota State University, Fargo, ND 58102, USA

ARTICLE INFO

*Article history:*
Received 14 December 2010
Received in revised form 4 February 2011
Accepted 7 February 2011
Available online 12 February 2011

*Keywords:*
Ni/YSZ SOFC anode degradation mechanism
Coal gas contaminants
Nickel antimony interaction
Antimony adsorption
Thermochemical calculations

ABSTRACT

The interactions of antimony with the nickel–zirconia anode in solid oxide fuel cells (SOFCs) have been investigated. Tests with both anode-supported and electrolyte-supported button cells were performed at 700 and 800 °C in synthetic coal gas containing 100 ppb to 9 ppm antimony. Minor performance loss was observed immediately after Sb introduction to coal gas resulting in ca. 5% power output drop. While no further degradation was observed during the following several hundred hours of testing, cells abruptly and irreversibly failed after 800–1600 h depending on Sb concentration and test temperature. Antimony was found to interact strongly with nickel resulting in extensive alteration phase formation, consistent with expectations based on thermodynamic properties. Nickel antimonide phases, NiSb and $Ni_5Sb_2$, were partially coalesced into large grains and eventually affected electronic percolation through the anode support. Initial degradation was attributed to diffusion of antimony to the active anode/electrolyte interface to form an adsorption layer, while the late stage degradation was due the Ni–Sb phase formation. Assuming an average Sb concentration in coal gas of 0.07 ppmv, a 500 μm thick Ni/zirconia anode-supported cell is not expected to fail within 7 years when operated at a power output of 0.5 W $cm^{-2}$ and fuel utilization above 50%.

Published by Elsevier B.V.

## 1. Introduction

High fuel flexibility is among the significant advantages of solid oxide fuel cells (SOFCs), allowing the direct use of fossil and bio fuels without a hydrogen separation unit. Other important advantages include high electrical efficiency, predicted to exceed 45% when operated on gasified coal, and low emissions [1]. Synthesis gas derived from coal and biomass, which consists of a mixture of hydrogen, carbon monoxide, carbon dioxide, and steam, may also contain finite amounts of tars and impurities such as S, Se, P, As, Sb, Cd, Pb, Cl, depending on fuel source. To remove the impurities, synthesis gas is commonly treated with a series of chemical processes and scrubbers. The level of purification compatible with long-term SOFC performance goals has been established for sulfur, phosphorus, arsenic and chlorine [2–7]. Similar information is needed for each impurity to establish cleanup criteria for coal gasifier plants intended to fuel multi-megawatt SOFC systems.

Antimony is widely distributed in coals, at concentrations of 0.05–10 ppmw across the world [8]. The average content of antimony in U.S. coals has been estimated at 1.2 ppmw [9], which corresponds to an average of ~0.07 ppmv in synthesis gas derived from coal [10]. Substantially higher concentrations have been reported for specific coal deposits: nearly 350 ppmw for a Late Permian coal from Inner Mongolia [11], nearly 2000 ppmw for brown coals from the Pavlovka deposits in Russia [12], more than 2300 ppmw for Middle Miocene bituminous coals from Turkey [13], and more than 3800 ppmw for a Late Permian coal from southwest China [14]. Antimony is found in several forms in coals, such as in pyrite substituted for iron or sulfur, or combined with dispersed sulfide particles in organic matter [11]. Antimony in coal primarily is volatilized during gasification [10,15], such that contact with the Ni/YSZ anode of an SOFC operated on coal gas is possible without pre-treatment.

The interaction of antimony with nickel has been studied in detail, mainly because of the extensive commercial use of Sb additives as passivating agents to the nickel catalysts in the catalytic crackers in refineries [16–18] to suppress the coke and hydrogen formation. The large negative heat of mixing, −33 kJ $mol^{-1}$ [19], indicates a strong interaction of antimony with nickel. Surface enrichment of antimony in dilute alloys with nickel has been observed, driven by a low surface free energy and large differences in ionic radii [19]. Antimony forms ordered structures when deposited onto Ni. At temperatures above 500 K, $p(\sqrt{3}\times\sqrt{3})R30°$–Sb/Ni(1 1 1) and

* Corresponding author. Tel.: +1 509 375 2337; fax: +1 509 375 2186.
*E-mail address:* olga.marina@pnl.gov (O.A. Marina).

0378-7753/$ – see front matter. Published by Elsevier B.V.
doi:10.1016/j.jpowsour.2011.02.027

$p(\sqrt{16}/7 \times \sqrt{16}/7)R19^\circ$–Sb/Ni(1 1 1) structures were observed by the low-energy electron diffraction (LEED) [20]. The catalytic properties of nickel are altered by antimony additions, and poisoning of hydrogen and CO chemisorption on Ni catalysts has been reported [21,22]. Goldwasser et al. [22] explained these observations in terms of an exothermic Ni–Sb alloy formation with surface enrichment in Sb. Parks [21] attributed antimony poisoning to: (a) geometric blocking of nickel sites by the antimony, (b) the modification of the electronic properties of Ni surface atoms by Sb, and (c) the equilibrium between Sb interacting with the support and with nickel determined the amount of Sb available to passivate the nickel. Antimony is expected to form secondary phases with Ni at parts per million concentrations in coal gas [23]. Ni–Sb compounds are intermetallics and have many other applications, for example, in various functional and thermoelectric materials due to their special physical and chemical properties. No effect on fuel cell performance was observed with up to 8 ppm Sb in coal gas by Bao et al. [24].

In the present work, the bulk and surface interactions of the Ni/YSZ anodes with antimony were studied both in anode-supported and in electrolyte-supported button cells, with the goal of establishing maximum permissible Sb concentrations in coal gas without significant impact on the SOFC lifetime. Because of the relatively thick anode support, an anode-supported cell design allows an assessment of any structural rearrangements that may have occurred during short-term and long-term exposures. Electrolyte-supported cells, due to a smaller nickel inventory, provide a more rapid response to the impurities. Additionally, Ni/YSZ coupons without electrical bias were evaluated in flow-by and flow-through arrangements. Extensive post-test analyses were performed to identify the reaction products and their distribution, revealing at least two principal modes of degradation. The experimental results were supported by thermochemical modeling.

## 2. Experimental

### 2.1. Button cell configurations

Both anode-supported and electrolyte-supported cells were employed in tests with antimony. Anode-supported button cells with an active area of 2 $cm^2$ were fabricated as described previously [6]. The Ni/YSZ support was approximately 0.9 mm thick and was comprised a Ni/YSZ bulk layer with a 40/60 vol.% solids ratio and approximately 30 vol.% porosity, and an approximately 7 μm thick active Ni/YSZ electrode layer with 50/50 solids vol.% Ni/YSZ. The electrolyte was 8 mol.% YSZ (8YSZ), approximately 7 μm in thickness. A 3 μm thick samaria-doped ceria (SDC) barrier layer was applied to the pre-sintered at 1375 °C anode/electrolyte structure by screen printing followed by sintering at 1200 °C. A 30–50 μm thick $(La_{0.80}Sr_{0.20})_{0.98}MnO_3$ (LSM-20) cathode was applied in the same manner and sintered at 1100 °C for 2 h. A NiO paste grid was screen-printed onto the anode to serve as the anode current collector and fired at the time as ceria layer together with Pt electrical leads pressed against the anode. The cathode current collector was Ag foil grid impregnated with Ag paste and sintered *in situ* during seal curing. Cells were sealed to alumina test fixtures with a barium aluminosilicate glass [25] by heating to 800 °C in air. To decrease possible interactions between electrical leads and antimony, anode leads were positioned outside the anode chamber coming out through the glass seals. The part of leads on the anode surface was coated with a barium aluminosilicate glass to limit the unwanted interactions with the gas environment and to reduce partial antimony consumption that may lead to an underestimate of deleterious effects. Three or four cells were configured in a single box furnace. The Ni/YSZ anode was reduced *in situ* at 800 °C in moist hydrogen with ca. 3% $H_2O$.

Electrolyte-supported button cells were purchased from Fuel Cell Materials (a division of NexTech Materials, Inc.) and were 25 mm in diameter, with 1.26 $cm^2$ active anode and cathode areas. These cells were comprised an 8YSZ electrolyte of $165 \pm 8$ μm in thickness, with a Ni/8YSZ anode approximately 30 μm in thickness. The cathode consisted of LSM-20, with a ~2 μm gadolinia-doped cerium oxide barrier layer between the cathode and the electrolyte. A nickel oxide current-collecting grid, approximately 5 μm in thickness, was screen printed onto the cells to facilitate electrical contact. Cells were sealed to alumina test fixtures with a barium aluminosilicate glass, similar to anode-supported cells. The anode leads were positioned again outside the anode chamber and the exposed parts of electrical leads were coated with the glass.

### 2.2. Cell testing

Cell tests were performed at 700 and 800 °C. The cell temperature was monitored by a thermocouple placed near the cathode surface. The fuel gas was either 10 vol.% $CO_2$-buffered hydrogen or synthetic coal gas. The synthetic coal gas was created by equilibrating 55 parts by volume hydrogen with 45 parts by volume carbon dioxide over a separate Ni/YSZ catalyst bed held at a constant temperature of 700 °C, yielding a nominal composition of $H_2$–CO–$CO_2$–$H_2O$ = 33–22–23–22 vol.%. The equilibrium gas composition was confirmed by measuring the open-circuit potential which is directly related to the $pH_2/pH_2O$ via the Nernst equation. Antimony vapor was added using a stable thermal evaporation source after the catalyst bed. A small alumina reservoir was filled with the Sb powder and inserted inside an alumina fixture onto which a fuel cell was mounted. A thermocouple, protected with a glass coating from any undesired interactions with the antimony, was attached to the bottom of this reservoir on the outer side to continuously control the temperature at which Sb powder was held. In the beginning of all tests, the Sb reservoir was held at room temperature to obtain the baseline cell performance on clean coal gas. To introduce Sb, the position of the reservoir was changed by elevating it into the hot zone and fixing at the given temperature to provide the desired Sb vapor pressure. The reservoir temperature was constantly monitored to keep the fluctuations at a minimum and recorded during all of the tests. The Sb vapor pressure was calculated as a function of temperature at the predetermined oxygen partial pressures using HSC Chemistry 6.12 [26]. The amount of dosed antimony was verified from the mass balance using a porous Ni/YSZ coupon in a flow-through arrangement as described below.

Prior to Sb exposure, all cells were pre-conditioned at 0.7 V and stable baselines were obtained for 24–150 h at a constant current or voltage, at which the following tests were performed. Most of the tests were performed at a constant current (0.1–1 A $cm^{-2}$) to provide the constant operating conditions to the cathode throughout the test duration, and some were also performed at a constant voltage of 0.8 V. Fuel utilizations in all test were low, <10%. The cathode was supplied with pure oxygen from a pressure swing adsorption unit to minimize the cathodic polarization contribution. Arbin Instruments multichannel controllers were used for dc electrochemical tests. A Solartron Model 1260/1287 potentiostat/frequency response analyzer combo was used to obtain ac electrochemical impedance spectra at random time intervals at the same bias current for all of the cells during exposures to antimony.

### 2.3. Coupon tests

As a complement to cell tests, coupons consisting of Ni/YSZ anode support material were exposed to synthetic coal gas with

antimony in the absence of an electrochemical bias. These tests were used to verify the amount of Sb vapor in respect to the calculated amount and as a screening tool to assess the tendency for Sb–Ni reactions. Tests were performed in a flow-by and flow-through arrangements for specific time, temperature, and Sb concentration. In flow-through tests, porous Ni/YSZ discs without a dense electrolyte and a current collecting grid were sealed onto alumina tubes with barium aluminosilicate glass, similar to procedures used for button cells. After NiO reduction, coal gas containing 1 ppm of antimony was forced to flow through the cermet coupon at a flow rate of 0.67 $cm^3\ cm^{-2}\ s^{-1}$ at 700–850 °C for ~75 h. The extent of reaction was assessed by electron microscopy, as described below. An important advantage of flow-through tests is that a mass balance could be established for contaminants that interacted strongly with the anode support. Such analysis was performed to verify the amount of Sb dosed in the fuel gas. In flow-by tests, porous Ni/YSZ coupons 2.5 cm × 5 cm in dimension were sealed onto an alumina fixture in a configuration similar to that of a cell within a planar SOFC stack. In this case, the coupon included a dense 7 μm-thick YSZ electrolyte layer to maintain gas tightness, though these coupons were not operated electrochemically. Coal gas containing 0.1 ppm or 1 ppm of antimony flowed lengthwise across the coupon at flow rates similar to those utilized in a stack.

### 2.4. Post-test analyses

After test termination, all of the cells and coupons were cooled to room temperature in dry hydrogen in the absence of Sb. Individual cells and coupons were mounted and metallographically polished to a final colloidal silica finish for subsequent microstructure analyses using a JEOL 7600F field emission gun scanning electron microscope. Scanning electron microscopy (SEM) analyses were performed in a wide beam current range from the picoamps for high resolution imaging to 10–100 nA for compositional and crystallographic analysis with probe sizes of 10 nm or less. Compositional analysis was conducted using energy dispersive spectrometry (EDS). X-ray elemental mapping was employed to determine elemental distributions and extent of phase transformation. Crystallographic information on the alteration products was obtained using an electron backscatter diffraction (EBSD) system by Nordlys. The samples were tilted at 70° to the electron beam to minimize the interaction volume to a 10–20 nm depth below the surface of the specimen.

Selected samples were analyzed by X-ray photoelectron spectroscopy (XPS) to evaluate whether a surface adsorption layer was present in regions not converted to bulk reaction products. XPS measurements were performed using a Phi 5000 VersaProbe. This system consisted of a monochromatic focused Al Kα X-ray (1486.7 eV) source and a hemispherical analyzer. The X-ray beam was incident normal to the sample and the emitted photoelectrons were collected at an emission angle of 45° relative to the sample normal. Wide scan data were collected using pass energy of 117.4 eV. High-resolution scans were obtained using pass energy of 23.50 eV. The XPS spectra were referenced to an energy scale with binding energies for Cu $2p_{3/2}$ at 932.67 ± 0.05 eV and Au 4f at 84.0 ± 0.05 eV. Low energy electrons at ~1 eV, 40 μA and low energy $Ar^+$ ions were used to minimize the surface charging. The XPS data were also collected following 2 kV $Ar^+$ sputtering over a 3 mm × 3 mm area of the specimen for 2 min. The sputter rate for 2 kV $Ar^+$ over a 3 mm × 3 mm raster area is determined to be ~6.5 nm $min^{-1}$ using $SiO_2$/Si reference material with known thickness from X-ray reflectivity and ellipsometry.

## 3. Results

### 3.1. Antimony concentration verification

Porous Ni/YSZ discs without electrolyte and current collecting layers were sealed onto alumina tubes and exposed to synthesis gas containing 10 or 100 ppm Sb in a flow-through configuration at 700 and 800 °C for 75 h. The extent of the Sb reaction with Ni and the depth of Sb penetration was assessed from polished cross-sections using SEM/EDS. It was found that antimony strongly reacts with nickel. A reaction product migrates to the surface in the form of Ni–Sb where it coalesces, while a devoid of nickel YSZ layer remains below the crystalline products. Using determined dimensions (penetration depth and alteration spot size), the total Ni surface area of isolated particles was calculated. From the known initial quantity of nickel per unit volume in the anode support and established by SEM/EDS the Ni–Sb phase composition and Sb penetration depth, the concentration of Sb was calculated. Experimentally obtained penetration depths were within 4% from the expected values. Thus, it was concluded that sublimation provided a reliable source of Sb.

### 3.2. Anode-supported cell tests

Anode-supported cells showed a rapid performance decrease followed by a new steady-state when antimony was added to synthetic coal gas. Figs. 1 and 2 show cell potentials at constant current at 700 and 800 °C for a set of anode-supported cells from the moment when different amounts of Sb were added to the fuel gas, as well as ohmic and electrodic losses derived from the impedance spectra collected at random time intervals during exposures Sb. At these temperatures, an almost immediate and small, ca. 20–60 mV, cell potential drop was observed in the presence of 1–9 ppm Sb compared to control cells in clean coal gas. The area specific resistance (ASR) of cells was increased by ~10–15% at 700 °C and 15–25% at 800 °C, which corresponds to a power output loss of less than 5% and indicates that a minor poisoning by Sb took place. Changes in ASR were essentially independent of Sb concentration and were reversible. When the Sb source was removed after several hours of testing, the cell resistance was slowly decreased to approximately the initial value, suggesting that Sb diffusion into the Ni bulk or Sb desorption may have occurred [27]. Only small changes in cell performance were observed during ~1600 h exposures to 1–9 ppm Sb at 700 °C and 600 h exposures to 1 ppm Sb at 800 °C. Prolonged operation with 8 ppm Sb at 800 °C caused more degradation: the ASR increased by more than a factor of 2 during the initial 200 h and increased even more sharply after 550 h of exposure. As seen in Fig. 2b, the ohmic resistance was not affected by 1 ppm Sb at 800 °C and the electrodic resistance increased by ~1/3 due to Sb exposure. Thus, the rapid ASR increase shown in Fig. 2a was due to a rise in electrodic (obviously, anodic) polarization losses. At higher Sb concentrations and longer reaction times, a significant increase in the ohmic resistance was also observed. Similar trends were observed in tests at 700 °C, but the ohmic component appeared to slightly decrease with time, Fig. 1b.

Fig. 3 shows the change in the cell ASR to the presence of antimony for varied current densities. The ASR was normalized to the initial value determined at the same current density prior the Sb addition. A cell resistance increase to the Sb presence was lower at higher current densities than at lower current densities, and the time to a new steady state was inversely proportional to the current density. Because the ohmic component was not affected as much by the presence of Sb during short exposures (Figs. 1 and 2), it is clearly the electrodic resistance that was responding to the Sb differently at different polarizations. Similar trends were observed at 700 °C, and cells operated at a lower current density exhibited relatively higher poisoning by Sb than those operated at higher current

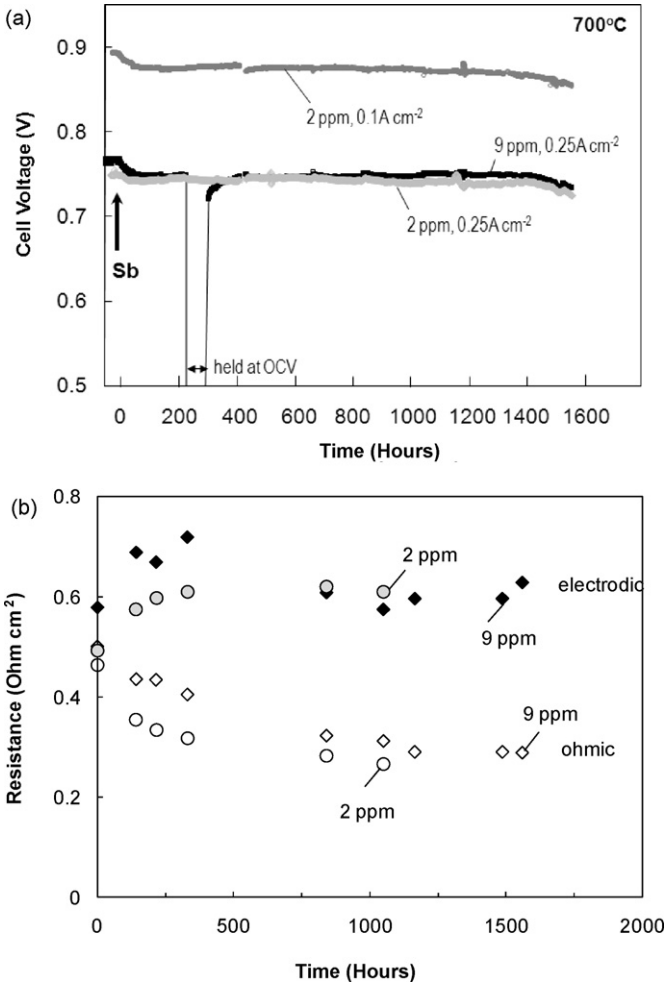


**Fig. 1.** (a) Performances of anode-supported cells in synthetic coal gas with 2 and 9 ppm Sb at 700 °C at a given current density and (b) electrodic and ohmic resistances derived from corresponding impedance spectra at a bias current of 0.25 A cm$^{-2}$. Time of Sb addition is moved to the origin.

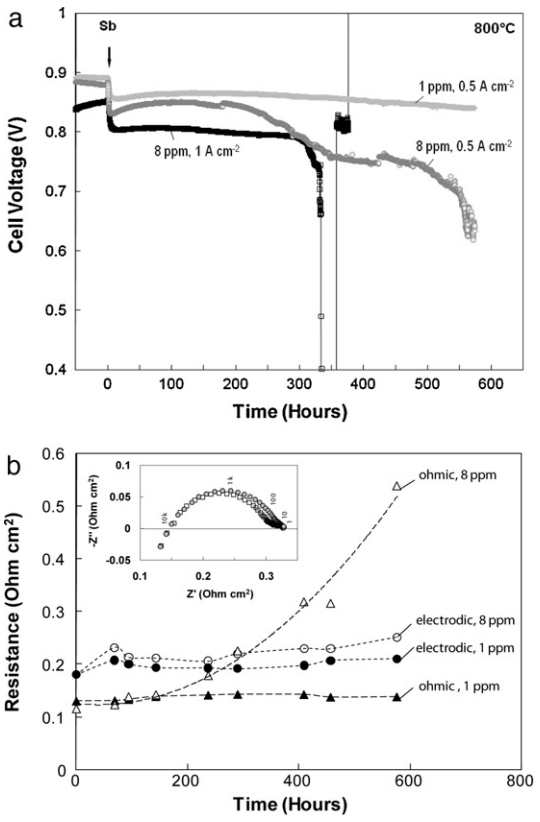


**Fig. 2.** (a) Performances of anode-supported cells in synthetic coal gas with 1 and 8 ppm Sb at 800 °C at a given current density and (b) electrodic and ohmic resistances derived from corresponding impedance spectra at a bias current of 0.5 A cm$^{-2}$. Time of Sb addition is moved to the origin. The inset illustrates complex impedance spectra obtained before and after the Sb addition.

densities. The Sb effect appeared to be less pronounced at 700 °C than at 800 °C, however. This is likely because other contributions to total cell resistance (i.e., cathodic polarization losses and ohmic losses) also were higher at lower temperatures, rendering effects due to Sb less visible.

Although the button cells used in the current work were not equipped with the reference electrodes, and the anodic contribution could not be easily isolated from the cathodic in entire polarization losses, some of the complex impedance spectra were fitted to an equivalent circuit as an attempt to qualitatively distinguish which process was contributing to the anode poisoning. For the tests performed at a constant current, it is reasonable to assume that the cathodic resistance was constant throughout the test. Any changes in the electrodic resistance should be attributed to the anodic response. The impedance spectra were fitted using the following equivalent circuit: $LR_0(RC)_1(RQ)_2(RQ)_3$, where $L$ is an inductance in series with $R_0$, an ohmic resistance, $(RQ)$ is a circuit consisting of a resistance and a constant phase element, and $(RC)$ is a circuit consisting of a resistance and a capacitance. The annotations 1, 2, and 3 indicate a time constant decrease. The quality of the fit was assessed by chi-square values of $<10^{-5}$. In clean coal gas only $R_1$ from a $(RC)_1$ circuit was slightly increased with time, while $R_0$ (ohmic), $R_2$, and $R_3$ from corresponding $(RQ)_2$ and $(RQ)_3$ circuits were nearly constant as the time progressed. $R_1$ was independent of the current density, while $R_2$ and $R_3$ decreased with the current increase, Fig. 4. When cells were exposed to 1 ppm Sb in coal gas, the absolute $R_2$ value did not change, while $R_1$ and $R_3$ increased, and $R_3$ increased the most. Such increase though was diminished at higher current densities.

### 3.3. Electrolyte-supported cell tests

Electrolyte-supported cells that were tested at 700 and 800 °C showed a response to Sb similar to that of anode-supported cells,

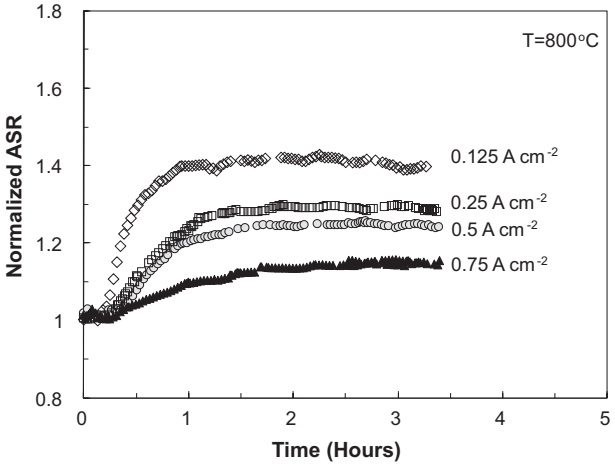


**Fig. 3.** Area specific resistances (ASR) of anode-supported cells calculated from the dc data obtained at various current densities during exposures to synthetic coal gas with 1 ppm Sb and normalized to those obtained in clean gas at 800 °C.

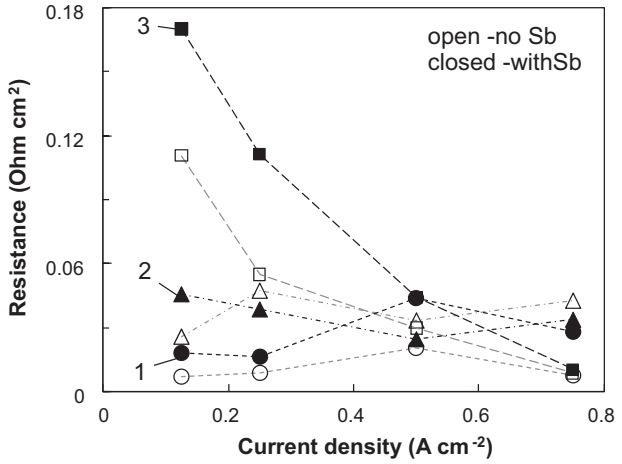


**Fig. 4.** Electrodic resistances, $R_1$ (circles), $R_2$ (triangles) and $R_3$ (squares), deconvoluted from the complex impedance spectra obtained from cells operated in clean synthetic coal gas (open symbols) and coal gas with 1 ppm Sb (closed symbols) at 800 °C at different bias currents.

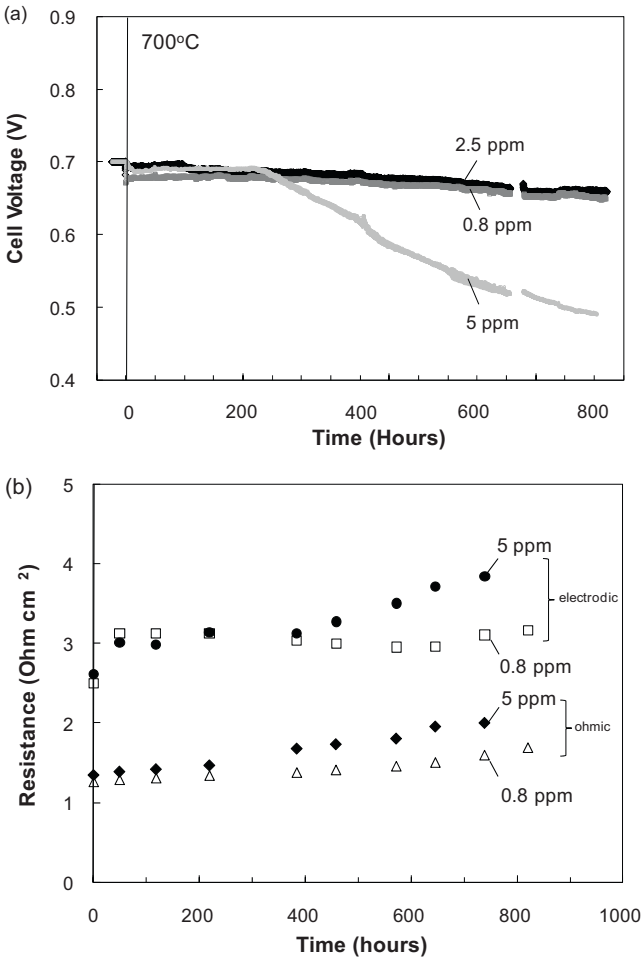


**Fig. 5.** Cell voltages at a constant current of 0.1 A cm$^{-2}$ (a) and electrodic and ohmic resistances (b) of the electrolyte-supported cells at 700 °C in synthetic coal gas with given concentrations of Sb. Resistances were derived from the complex impedance spectra obtained at a bias current of 0.1 A cm$^{-2}$. Time when Sb was added was moved to the origin. Data around 650 h were not collected because of the software malfunction.

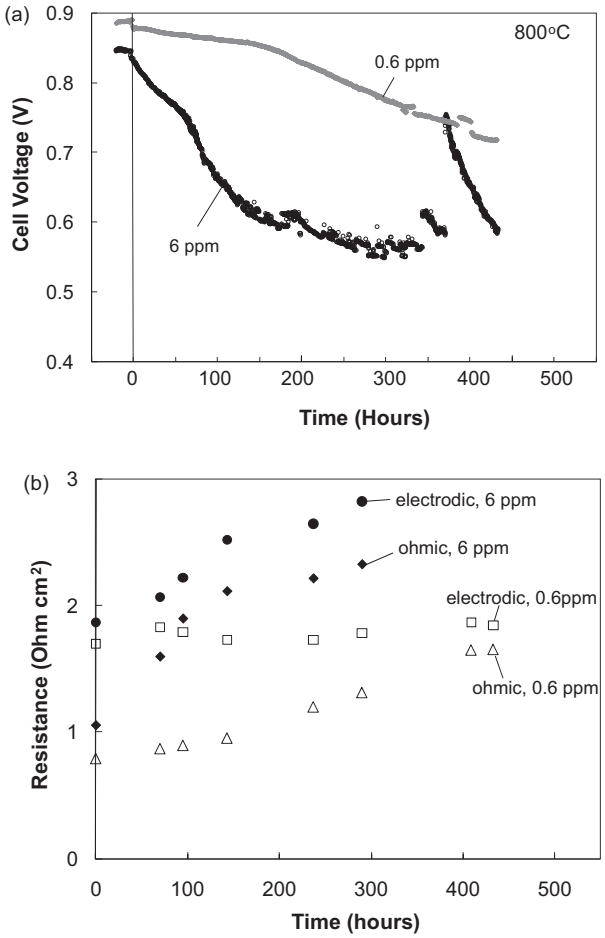


**Fig. 6.** Cell voltages at a constant current of 0.1 A cm$^{-2}$ (a) and electrodic and ohmic resistances (b) of the electrolyte-supported cells at 800 °C in synthetic coal gas with given concentration of Sb. Resistances were derived from the complex impedance spectra at a bias current of 0.1 A cm$^{-2}$. Time when Sb was added was moved to the origin.

though degradation occurred more quickly. Figs. 5 and 6 show cell voltages for a set of electrolyte-supported cells from the moment at which different amounts of Sb were added to the fuel gas. Also shown are corresponding resistances derived from the impedance spectra that were collected at random time intervals at the same bias current as the dc measurements. At 700 °C, an almost immediate but small, ~20 mV, drop in cell voltages was observed in the presence of Sb that was reversible, i.e., cell voltage recovered when the Sb was removed from the fuel gas after short (few hours) exposures. Over the following 650 h of continuous exposure to 0.8 and 2.5 ppm Sb little further changes were observed, while substantially more degradation was observed with 5 ppm Sb for exposures greater than 200 h, Fig. 5a. Ohmic and electrodic losses during exposures to 0.8 and 5 ppm Sb were separated from the impedance data and are given in Fig. 5b. As was observed for anode-supported cells, the electrodic resistance rose quickly with exposure to 0.8 ppm Sb, but remained essentially constant thereafter. Identical changes in the electrodic resistance were observed for a cell exposed to 5 ppm Sb for approximately 400 h, after which electrodic resistances started to increase. Ohmic resistances increased slowly with Sb exposure, at a rate approximately proportional to Sb concentration.

Electrolyte-supported cells exposed to Sb at 800 °C showed more rapid degradation than those at 700 °C under otherwise identical conditions. Results for cells exposed to 0.6 and 6 ppm Sb are shown in Fig. 6. Ohmic losses increased more than electrodic

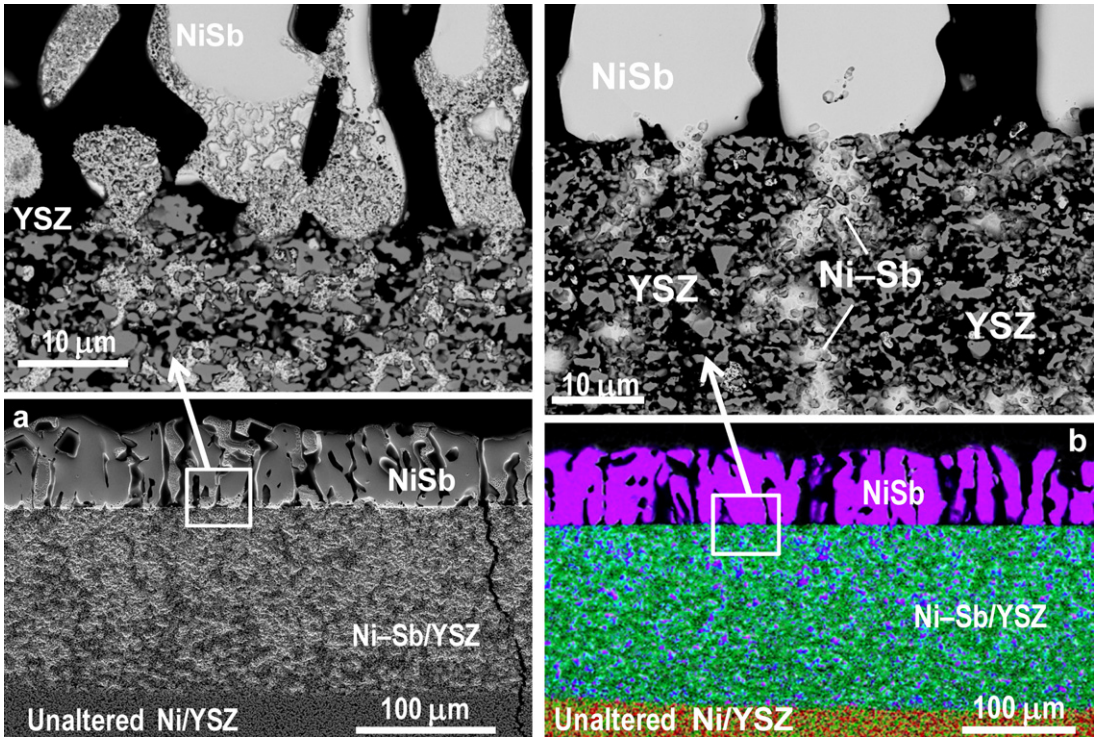


**Fig. 7.** Cross sectional SEM images and an X-ray elemental color map of the upper part of anode-supported cells after exposure to (a) 1 ppm and (b) 9 ppm Sb for 1560 h at 700 °C. Images are positioned such, that the fuel gas entered from the top perpendicular to the surface. The Ni from Ni/YSZ has reacted with Sb and migrated to the surface to form large NiSb crystals shown in light gray (or purple in the color mix map). The Ni–Sb phase inside the anode support is a mixture of NiSb, $Ni_5Sb_2$, and $Ni_3Sb$ phases. The Ni–Sb/Ni boundary is not as sharp as pictured due to minor Sb penetration below the regions of visible transformation. The YSZ is dark gray or green, Ni is gray or red, and the pores are black. (For interpretation of the references to color in this figure legend, the reader is referred to the web version of the article.)

losses for a cell exposed to 0.6 ppm, while electrodic and ohmic loss increases were similar for a cell exposed to 6 ppm Sb. Rates of performance loss slowed down with exposure time, reaching an apparent steady-state (where the cell ASR was doubled) in about 200 h. After approximately 350 h, sudden sporadic voltage increases and decreases occurred, Fig 6a. Both electrodic and ohmic resistances are seen to progressively increase with time, Fig. 6b. Similarly to the anode-supported cells, Sb poisoning of the electrolyte supported cells decreased with increased current density. The rate of the anode recovery after short term exposures to Sb seemed to be faster at higher current densities as well.

### 3.4. Post-test anode characterization

#### 3.4.1. Anode-supported cells

Post-test characterization of the Ni/YSZ anodes after exposures to Sb was performed using SEM/EDS and EBSD techniques. Fig. 7 shows typical SEM images of the upper part of the anode-supported cells after prolong exposures to Sb, where Ni–Sb interactions led to the Ni–Sb phase formation accompanied by severe agglomeration and coalescence. The size of the Ni–Sb crystallites ranged from 3 to 7 μm inside the anode support to several hundred microns on the anode surface. Reaction products at the anode surface were in the form of columnar crystallites, up to 80 μm after tests with 1 ppm Sb at 700 °C and up to 160 μm after tests at 800 °C. The crystallite size generally increased with Sb concentration and time of exposure. The EDS analysis determined the presence of $48 \pm 4$ at.% Sb in this phase, thus it was attributed to NiSb. EBSD analysis confirmed the presence of NiSb. Moreover, because the EBSD diffraction patterns did not change orientation when the electron beam was scanned across the particles and only occasional grain boundaries were found, most of these particles are likely to be single crystals. Because of the strong interactions, a rather sharp boundary between the altered and unaltered Ni/YSZ inside the anode support was clearly observed, similar to that observed in tests with phosphorus and arsenic [5,6]. Minor penetration of Sb below the region of visible transformation was limited to a few microns. While the main altered phase was NiSb, because

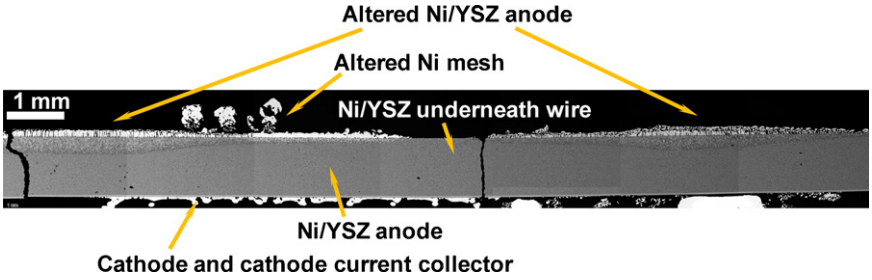


**Fig. 8.** Cross sectional SEM image of the part of the anode-supported cell illustrating the "shielding effect". The Ni/YSZ area below the current collecting wire, initially present in the center and removed prior to the SEM analyses, is not altered. The unprotected Ni/YSZ area around is affected by Sb to form large NiSb crystallites. Cracks occurred after the test during cell dismounting.

of the Sb concentration decline toward the boundary between converted and unconverted regions, other Ni–Sb phases, $Ni_5Sb_2$, $Ni_3Sb$ and solid solution were likely present. All three compounds, $Ni_3Sb$, $Ni_5Sb_2$ and NiSb, were identified in the converted part of the anode support by EBSD analysis. Similar morphologies were observed on samples tested at 800 °C. Although the test duration at 800 °C was a factor of 3 shorter than that at 700 °C, approximately similar amounts of the NiSb phase were revealed by the SEM analysis, indicating stronger interactions at higher temperatures.

For the test durations in this study, no morphological changes at the active anode/electrolyte interface of the anode-supported cells were observed. Because of the time dependence, one could project that for longer exposures above 1000 h, especially to Sb concentrations as high as 9 ppm, the Ni–Sb phase would reach the active anode and not be limited to the top ~200–300 μm layer, Fig. 7. This was observed during the interaction of the nickel anode with phosphorus, when all nickel in the 900 μm thick anode support was converted to a mixture of the Ni–P phases during a 1000 h test with 10 ppm $PH_3$ in coal gas [5]. However, this did not happen with Sb. Furthermore, not all Sb was captured in reactions with the nickel that was still present in the Ni/YSZ support in large amounts. This was evidenced by the observation of Sb in metallic form on the alumina holder near the gas exit after the test termination, and the gas exit was considerably cooler than operating cells. The level of the Sb concentration in the gas feed was verified independently by the flow-through coupon tests as described above, and the "excess" of Sb cannot not be attributed to the deviations in Sb dosing.

The presence of any obstacles between the solid Ni and the gaseous Sb caused a "shielding effect", similar to that observed in phosphorus and arsenic studies [5,6], and the Ni below "the shield" was not altered, while the other, unprotected, Ni was converted to the Ni–Sb. This is illustrated in Fig. 8, where the area below the current collecting wire that was in the middle (and was intentionally removed prior to the SEM analysis) is seen to remain unchanged, while the surface outside the shielded zone and the anode bulk was significantly affected. The wire itself was protected by a glass coating to avoid possible interactions with Sb identified previously [28] and no interactions between the wires and Sb were observed in the current study. No interactions between barium aluminosilicate glass and Sb were distinguished by SEM/EDS as well.

### 3.4.2. Electrolyte-supported cells

Figs. 9 and 10 illustrate the Sb distribution in the Ni/YSZ anodes of the electrolyte-supported cells after testing in synthetic coal gas with various concentrations of Sb at 700 and 800 °C. The anodes tested with Sb formed large Ni–Sb crystals on the surface, indicating strong Ni–Sb interactions. Based on the X-ray elemental maps, the anode layer just below these crystals was altered progressively depending on the Sb concentration, temperature and test time and the Sb distribution inside the anode was not uniform, Figs. 9 and 10. A summary of EDS analyses of anodes tested at 700 °C is shown in Fig. 11. Only single phase NiSb was found throughout the anode (together with YSZ) for cells exposed to 5 ppm Sb, whereas the Ni transformation in cells exposed to 0.8 and 2.5 ppm Sb was not as complete, and a mixture of NiSb, $Ni_5Sb_2$ and $Ni_3Sb$ with some amount of a Ni–Sb solid solution near the YSZ electrolyte was identified. The presence of three compounds, $Ni_3Sb$, $Ni_5Sb_2$ and NiSb, was further confirmed by the EBSD analysis. The anode morphology was significantly affected, especially during long-term tests with higher Sb concentrations, and the electrical network continuity was compromised. Antimony was associated only with the Ni and no Sb–YSZ compounds were found. Similar to tests with anode-supported cells, some unreacted Sb was found on the alu-

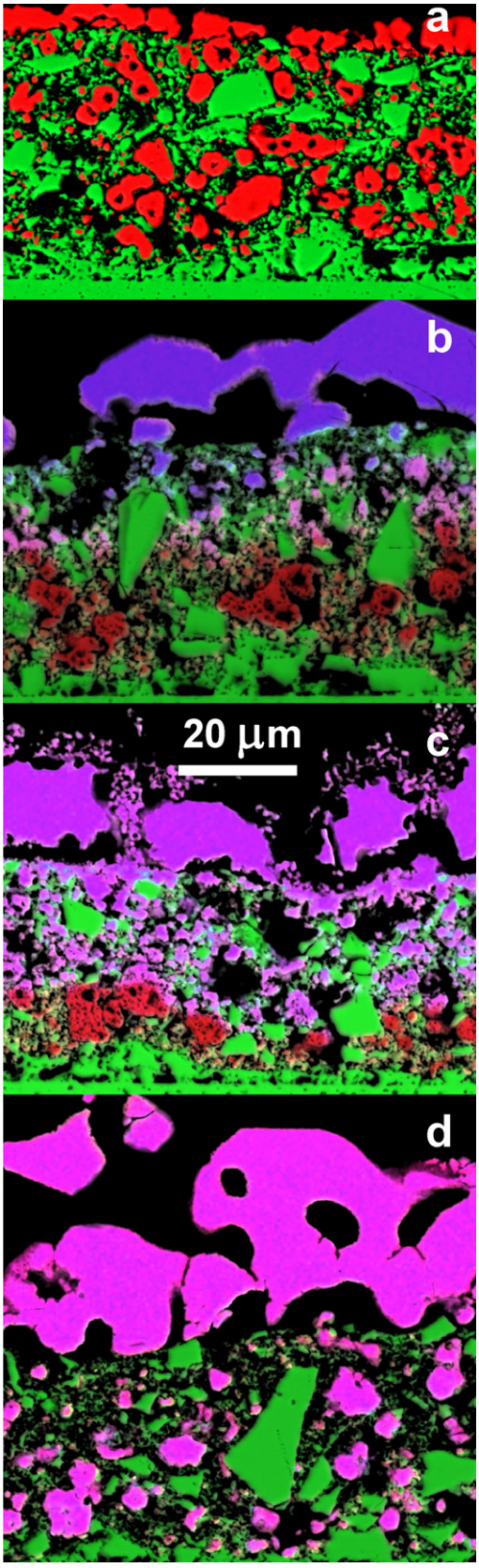


**Fig. 9.** SEM elemental maps obtained from cross sections of Ni/YSZ anodes in electrolyte-supported cells tested for 820 h at 700 °C in (a) clean synthetic coal gas, synthesis gas with (b) 0.8 ppm, (c) 2.5 ppm Sb, and (d) 5 ppm Sb. Ni is shown in red, YSZ is green, and Sb is blue. The Sb penetration and Ni–Sb phases (appear in pink/purple due to mixing of red and blue) coalescence are seen to progress with Sb concentration. (For interpretation of the references to color in this figure legend, the reader is referred to the web version of the article.)

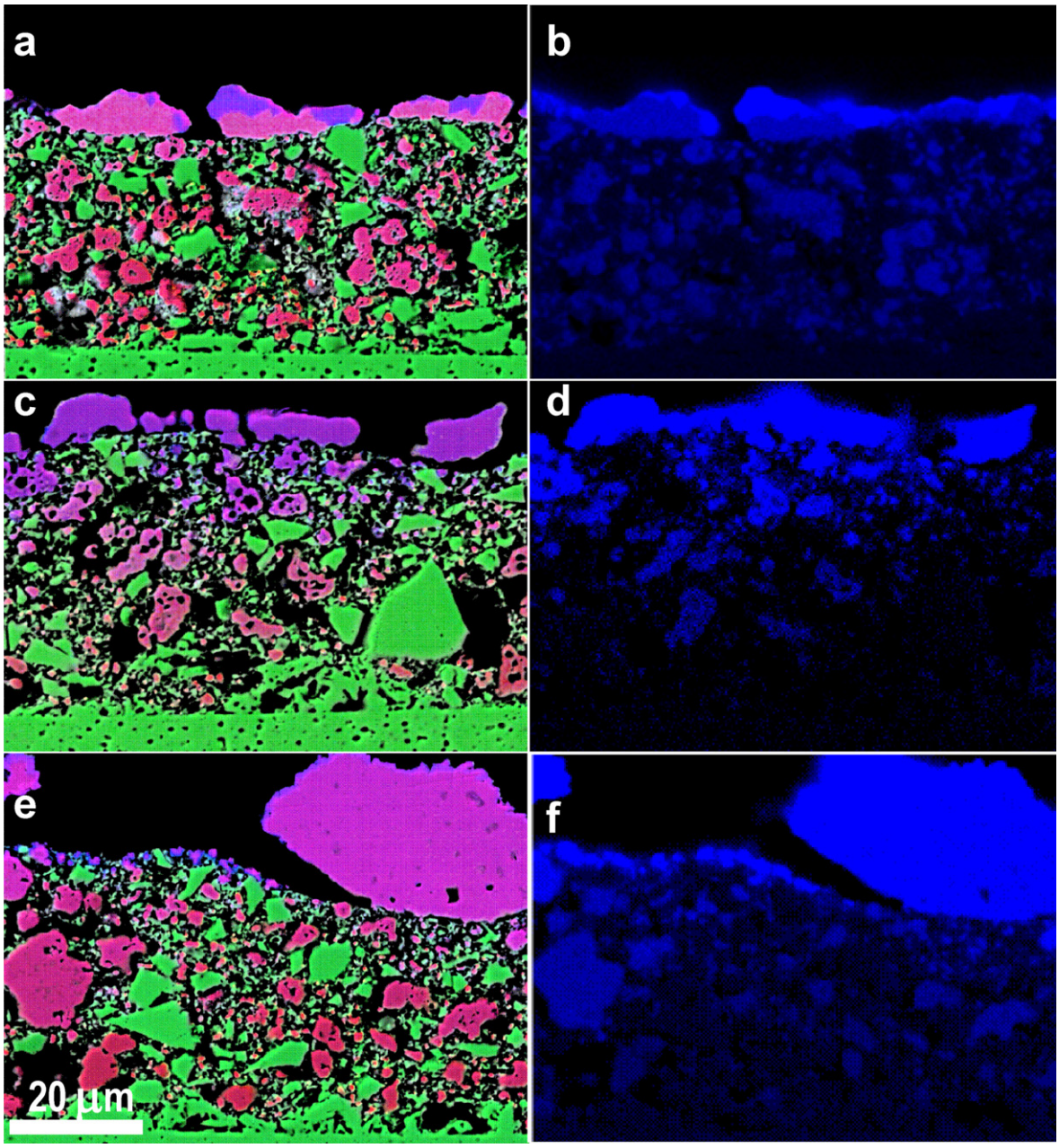


**Fig. 10.** SEM elemental maps obtained from cross sections of Ni/YSZ anodes in electrolyte-supported cells tested for 440 h at 800 °C in synthetic coal gas with (a, b) 0.6 ppm, (c, d) 2 ppm, (e, f) 6 ppm Sb. Ni is shown in red, YSZ is green, Sb is blue, and Ni–Sb appears pink/purple as a combination of red/blue. The corresponding Sb distribution (blue) in Ni/YSZ (black) is shown separately in (b, d, f). (For interpretation of the references to color in this figure legend, the reader is referred to the web version of the article.)

mina tubes near the outlet indicating incomplete capture of Sb by the anode.

### 3.5. Flow-by Ni/YSZ coupon tests

In flow-by tests, porous Ni/YSZ coupons 2.5 cm × 5 cm in dimension were sealed onto an alumina fixture in a configuration similar to that of a cell within a planar SOFC stack. In this case, the coupon included a dense 7 μm-thick YSZ electrolyte layer to maintain gas tightness, but was not operated electrochemically. Synthetic coal gas containing 0.1 or 1 ppm Sb flowed lengthwise across the coupon at flow rates similar to those utilized in a stack. As seen in Fig. 12, strong interactions between Sb and nickel resulted in effective capture of Sb at the cell inlet and secondary phase formation. The uptake was non-uniform along the cell length and limited to a distance of few millimeters from the gas inlet.

### 3.6. XPS analysis

Following the exposure to 1 or 10 ppm Sb for 2 h and rapid cooling in dry hydrogen without Sb, the surface of the Ni/YSZ coupon was analyzed by XPS. XPS, a technique sensitive to the outer few atom layers of the sample surface, detected Sb, Fig. 13, even though no solid Sb reaction products were found by SEM. XPS spectra were resolved into peaks corresponding to Sb $3d_{5/2}$ and Sb $3d_{3/2}$. As verified by the control Ni/YSZ samples tested without Sb, Fig. 13, Sb $3d_{5/2}$ was overlapped with O 1s. Thus, peak areas of Sb $3d_{3/2}$ with no O 1s overlap were used to quantify the Sb concentration. Antimony on the nickel surface was present in both metallic and oxidized

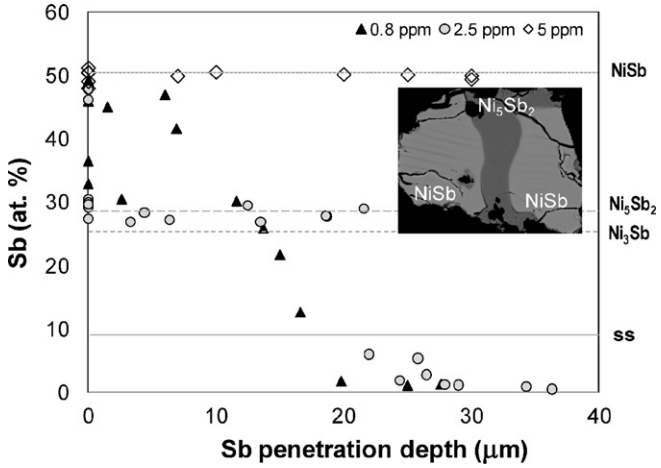


**Fig. 11.** Sb penetration into the 35 μm thick Ni/YSZ anode in electrolyte-supported cells after 820 h test at 700 °C with 0.8, 2.5 and 5 ppm Sb in coal gas. The amount of Sb in solid solution (ss) and possible Ni–Sb phases are suggested by gray lines. Inset illustrates the presence of two Ni–Sb compounds on the anode surface, one with 49 ± 1 at.% Sb and another with 29 ± 1 at.% Sb. Twinning and cracks inside the crystal indicate on stresses during the crystal growth.

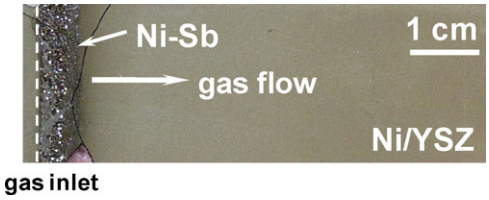


**Fig. 12.** Digital image of the part of the Ni/YSZ flow-by coupon after 560 h exposure to synthesis gas with 0.1 ppm Sb at 800 °C. Coupon cracked during disassembly and not during testing.

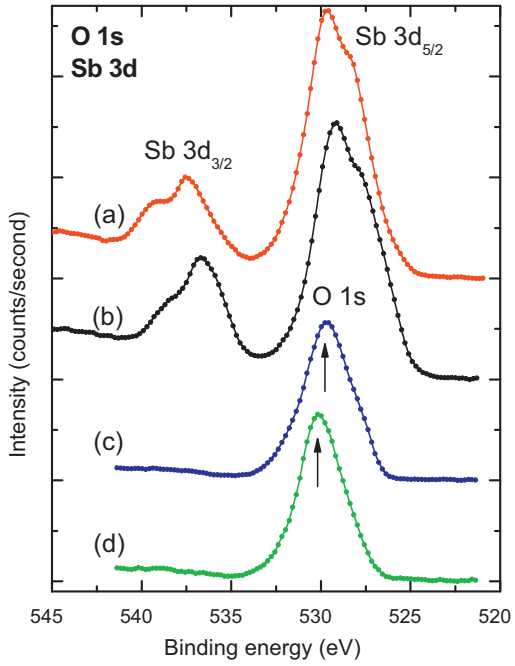


**Fig. 13.** O 1s and Sb 3d X-ray photoelectron spectra collected from the Ni/YSZ surface exposed to 10 ppm Sb for 2 h (a) before and (b) after $Ar^+$-sputter with 2 kV and 1.5 μA on 3 $mm^2$ area for 2 min. The spectra from the Ni/YSZ surface not exposed to Sb (c) prior to and (d) following $Ar^+$-sputter for 2 min are also included for comparison. The O 1s spectra overlap with Sb $3d_{5/2}$ spectra.

state: the lower binding energy peak at ~528 eV was from metallic or alloy phase of Sb, and the oxide form of Sb appeared as a shoulder at ~530 eV. Removal of an outer ~10 nm layer by sputtering suppressed the appearance of the oxidized form. Since no special care to isolate the Ni/YSZ coupon surface from the air environment at room temperature was taken once the sample was cooled (in hydrogen), the appearance of an oxidized form of Sb is likely the result of an air exposure. Because of this, no attempt to identify the Ni state was made. The Sb concentration on the surface was 23.2 at.% prior sputter and 17.9 at.% after a sputter. After brief exposure to 1 ppm Sb, a Sb concentration of 8.7 at.%, which is close to the antimony solubility limit in nickel, was determined.

## 4. Discussion

### 4.1. Thermochemical calculations for nickel–antimony system

The phase diagram for the nickel–antimony system is quite complex, with multiple intermediate phases possible [29–31]. Phases of potential importance to SOFC anode interactions include Ni(Sb) solid solution (Ni(ss)), $Ni_3Sb$, $Ni_5Sb_2$, and NiSb, all of which were identified in post-test analyses with SEM/EBSD. An additional phase $Ni_7Sb_3$ forms only at temperatures less than 582 °C, so is unlikely to be encountered. The phase NiSb exhibits the lowest enthalpy of formation of all intermediate phases in the Ni–Sb binary [31], and was found in greatest abundance in this study. Sources are not in complete agreement for the Ni–Sb system: Okamoto et al. [29] show $Ni_5Sb_2$ solid solution persisting to high temperatures, whereas Cao et al. [30] and Zhang et al. [31] show greater stability for $Ni_3Sb$ at high temperature.

This system exhibits quite high solid solubility of antimony in nickel at 9.0 atomic percent at 800 °C, which has been reported to alter the catalytic properties of nickel [16] and should certainly lead to changes in the electrocatalytic activity of the anode. Results obtained using SEM/EDS for anodes exposed to ~1 ppm Sb for less than 10 h are consistent with this solubility, as were results obtained by XPS following light ion milling to remove the outer few atom layers. A considerably higher surface concentration of Sb (>20%) was found by XPS prior to ion milling, consistent with reports that Sb tends to surface segregate on Ni [21,22]. Through surface segregation, low level exposure to a given adsorbate can have a disproportionately large effect on catalytic properties. While XPS data suggest that adsorbed Sb was present on the Ni surface in both oxidized state and metallic states, this information is not accurate as the XPS analyses were performed *ex situ* with no special care taken to protect the surface from air exposures at room temperature. Sb oxidation most likely has occurred post-experiment because only metallic Sb is expected to be present in a solid solution Sb.

Phase boundaries for the formation of NiSb versus temperature at several different fuel utilizations are given in Fig. 14. These calculations were performed using HSC 6.12 [26], with the following modifications to the database. Data for the gas species $SbO_2H_2(g)$ was added following Heams et al. [32]; this species was identified by Trembly et al. [23] as predominant in coal gas containing Sb, whereas Bao et al. [24] identified SbO(g) as the predominant Sb-containing gas species under similar conditions. Further, the enthalpy of formation for SbO(g) was modified in accordance with the Landolt–Börnstein database [33]. With these changes, the predominant gas species over a wide range of temperatures and levels of fuel utilization was $SbO_2H_2(g)$. Only at the 100% fuel utilization did $SbO_2H_2(g)$ and $Sb_4O_6(g)$ activities became comparable. Phase boundaries for solid phases Ni(Sb)ss, $Ni_3Sb$, and/or $Ni_5Sb_2$, all of which are solid solutions, were not calculated because of a lack of thermodynamic data, but may be expected to form at even lower Sb activities.

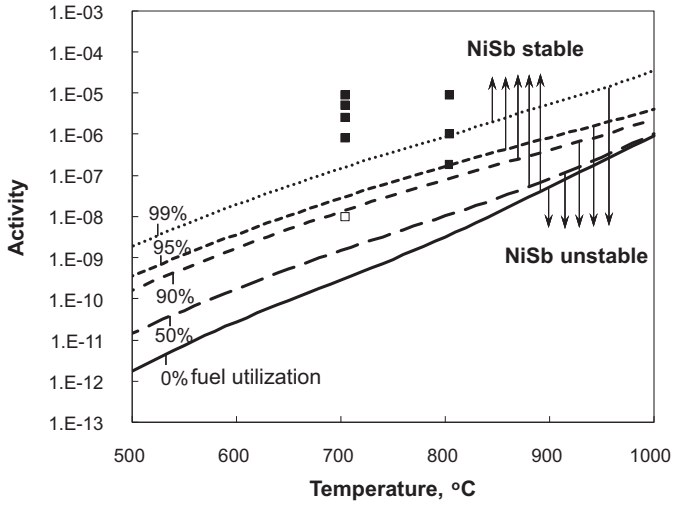


**Fig. 14.** Estimated minimum antimony activity in the synthetic coal gas required to form the phase NiSb at various (0, 50, 90, 95, and 99%) fuel utilizations. The filled squares indicate the Sb activity where NiSb was observed experimentally together with metallic Ni. Only at 0.01 ppm Sb no NiSb was observed (open square), maybe due to insufficient exposure time. Alteration phases $Ni_3Sb$ and $Ni_5Sb_2$ are expected to form at lower pressures than NiSb, though a lack of standard free energies for those compounds prevented a calculation of critical pressures required for formation.

Included in Fig. 14 are experimental observations for the formation of the alteration phase NiSb, which correspond to a fuel utilization of less than 10%. Filled symbols indicate that at least some NiSb was observed; some metallic Ni remained in all cases though would be expected to be consumed by reaction given sufficient exposure to Sb at indicated concentrations. It is predicted from the thermochemical calculations that a minimum gas phase concentration of antimony of ~0.5 ppb and 5 ppb is needed to form NiSb in coal gas at 700 °C and 800 °C, respectively, for 0% fuel utilization. One of the experimental points corresponding to exposure to 10 ppb Sb is unfilled in Fig. 14, which may simply be due to insufficient exposure time rather than thermodynamic instability.

That the stability of NiSb is expected to decrease with increased fuel utilization, as shown in Fig. 15, is an important finding and quite different from behavior that we have reported due to P, As, and especially Se exposure [5,6,34]. For Se exposure, we have found that high anodic polarization can result in the formation

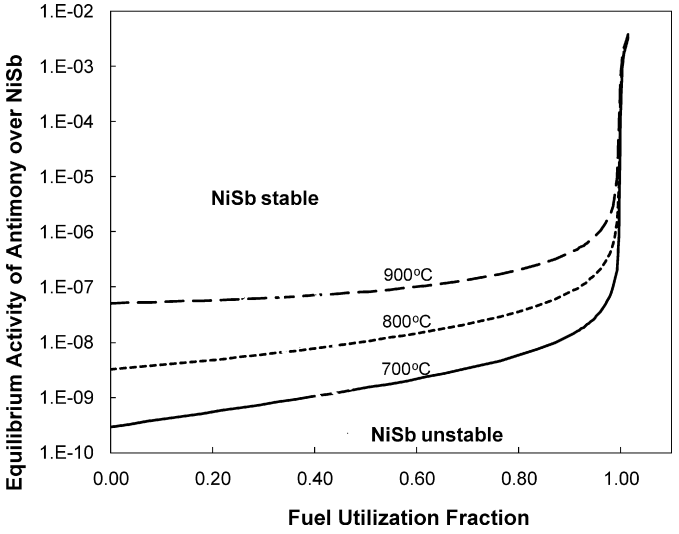


**Fig. 15.** Estimated antimony activity in the gas phase required to form the phase NiSb.

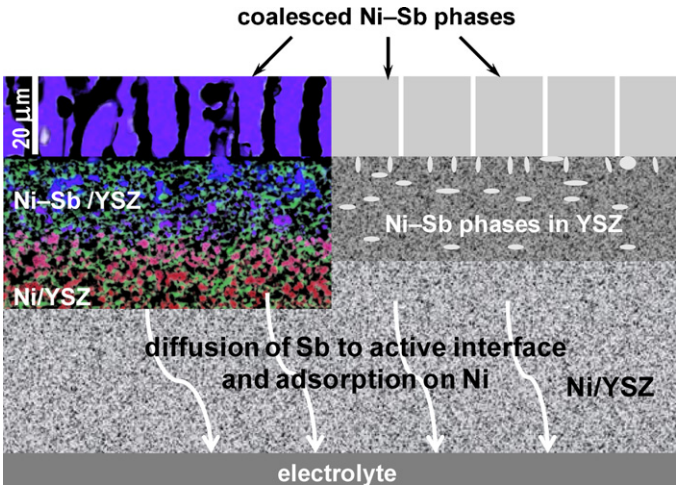


**Fig. 16.** Schematic diagram of the reaction of the Ni/YSZ anode with antimony in coal gas. Ni–Sb phases form in outer portions of the anode support, as illustrated by an SEM image in the upper left corner (anode-supported cell after 1560 h operation on coal gas with 1 ppm Sb at 700 °C). Surface diffusion of antimony to the active interface occurs as well, which is responsible for initial performance losses.

of nickel selenide phases at the active interface, at $H_2Se$ concentrations well below those needed to form alteration phases elsewhere in the anode support [34]. Locally high fuel utilization at the anode/electrolyte interface can result from high anodic polarization. Similarly, Kishimoto et al. predicted that high anodic polarization could lead to nickel sulfide formation at the active interface but nowhere else within the anode [35]. For Sb exposure, high current densities render NiSb and perhaps other reaction products less likely to form.

### 4.2. Proposed cell degradation and failure mechanism

Two principal processes contribute to the Ni anode deactivation and degradation in the presence of Sb: (1) adsorption of Sb onto Ni surfaces, which lowers the electrocatalytic activity of the anode, and (2) reaction of Sb and Ni to form binary alloys, which leads to coalescence of Ni within the anode support and possible loss of electrical connectivity. These processes are summarized schematically in Fig. 16.

#### 4.2.1. Initial stages of degradation – surface adsorption of Sb on Ni

Both anode- and electrolyte-supported cells rapidly responded to Sb present in the synthesis gas and a new, less active steady state was established. This rapid electrochemical response suggests fast Sb transport to the triple phase boundary and adsorption on the Ni sites that are active in the electrochemical fuel oxidation. Such responses were similar to those due to exposure to $H_2S$ or $H_2Se$, but the absolute voltage drop at a given current density was much smaller in the present study. Adsorption was reversible: when the Sb source was removed from the fuel gas in a couple of hours, the cell resistance slowly returned to the initial value. Although no Ni–Sb secondary bulk phases at the active anode/electrolyte interface for the test duration were observed in post-test analyses, XPS analyses confirmed that adsorbed Sb species were in metallic form rather than oxidized. Further, XPS analyses showed a surface concentration of Sb on Ni well in excess of the solid solubility limit, consistent with Sb surface segregation as observed previously [21,22]. Thus, initial reaction products were limited to surface adsorption layers and solid solution formation [27].

Initial changes in polarization resistance were principally electrodic in nature, were independent of the Sb concentration, and

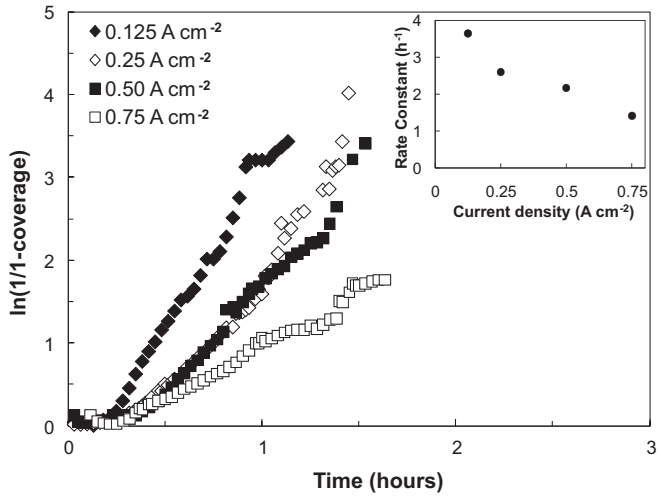


**Fig. 17.** Changes in relative coverage with time, as derived from the data obtained at different current densities from Fig. 3. Fitted first order rate constants calculated from the slopes are shown as an inset.

were affected by current density. From electrochemical impedance measurements, the major resistance increase occurred in the high frequency impedance arc that is usually related to the charge transfer processes in the anode. With longer exposures, changes in mid-frequency process (similar to those with phosphorus [5]) became obvious and could be due to the diffusional limitations. Independence with respect to the Sb concentration during initial exposure relates to the formation of a monolayer, identified in previous studies as $p(\sqrt{3}\times\sqrt{3})R30^\circ$–Sb/Ni(1 1 1) and $p(\sqrt{16/7}\times\sqrt{16/7})R19^\circ$–Sb/Ni(1 1 1) structures using LEED [20]. With continued exposure, multilayer adsorption and the formation of new solid phases is possible, depending on the activity of Sb in coal gas. Finally, we observed that both the rate of increase in cell resistance due to Sb adsorption and the steady state resistance decreased with increased current density. Fig. 17 shows first order changes in relative coverage versus time, derived from the data of Fig. 3, where it is assumed that the plateau reached within ~3 h corresponds to full coverage. Rate constants calculated from the slopes are included as an inset in Fig. 17, and show a strong inverse dependence on current density.

#### 4.2.2. Late stages of degradation – formation of solid reaction products

As the time of exposure progressed, a second stage of degradation became apparent where performance losses increased substantially, sometimes to the point of complete cell failure. Extensive formation of solid reaction products, particularly NiSb, was observed on the surface of the anode and within the anode support. From impedance spectroscopy results, it is clear that increases in ohmic losses were dominant. Since the electrical conductivity of NiSb is high [36], the most probable explanation involves the loss of the electrical conduction path between the particles (percolation loss), similar to that observed in tests with phosphorus [5] and arsenic [6]. Abrupt performance losses and gains (Figs. 1, 2 and 6a) also support the electrical percolation loss/gain mechanism. Lack of continuity between NiSb particles could be seen in Figs. 7 and 9.

An intrinsically lower activity of Ni–Sb phases toward the electrochemical fuel oxidation can be eliminated as a possible explanation for these observations, especially given that NiSb was never formed within the active anode of an anode-supported cell. Further, while solid reaction products were formed at the anode/electrolyte interface of electrolyte-supported cells, the NiSb phases retained moderate activity for the fuel oxidation. Despite most of the anode layer being converted to NiSb, as shown in Fig. 9c and d, only small performance losses ensued, Fig. 5. The electrocatalytic activity of the Ni and Ni–Sb anode cannot be compared directly: in the electrolyte-supported cells where Sb did reach the triple phase boundary, substantial morphological changes inside the active anode also became apparent and likely were responsible for the irreversible degradation.

As determined by the SEM/EDS and EBSD analyses, $Ni_3Sb$, $Ni_5Sb_2$, and NiSb, were present in the anode support of the anode-supported cells and coalesced into large grains on the surface or much smaller crystals inside the anode support. In such cells, the Ni–Sb agglomeration was different from that observed for Ni–As and Ni–P, where large agglomerates inside the anode support caused numerous stresses and cracks and caused cell failure [5,6,37]. Considering the Ni and NiSb densities of 8.902 g cm$^{-3}$ and 8.74 g cm$^{-3}$ at 25 °C, respectively, the volume change on Ni conversion to NiSb is substantial, >300%. The large difference should contribute to large volume expansion and enormous stress created within the anode support. Indeed, twin structures, sheer effect, twining, and deformation, and splitting one metal particle into several, all indicative of stress, were observed, especially with the electrolyte supported cells. As illustrated in the inset in Fig. 11, some Ni–Sb particles had numerous cracks, which is indicative of stress, and some consisted of two phases.

### 4.3. SOFC stack life predictions

Without cleanup, the average concentration of Sb in coals worldwide is sufficiently high such that interactions with the Ni anode of an SOFC are expected. The average concentration of Sb in U.S. coals is 1.2 ppmw [9], corresponding to ~0.07 ppmv in synthesis gas derived from coal [10]. Substantially higher Sb concentrations are found in certain deposits, however. Antimony is expected to interact with the Ni anode in two principal ways: formation of a surface adsorption layer, which results in small and reversible performance losses, and formation and coalescence of binary Ni–Sb solid phases, which can lead to cell failure through loss of electrical connectivity in the anode support and is of greatest importance. At 800 °C and low fuel utilization typical of the fuel inlet, the minimum Sb activity in coal gas needed to react to form binary Ni–Sb solid phases is approximately an order of magnitude smaller than the expected average concentration in coal gas. That minimum Sb concentration decreases with increased temperature and with increased fuel utilization.

The time required to form an adsorption layer of Sb on Ni is quite short. Assuming an average nickel particle size of 1 μm and an anode thickness of 500 μm, the surface area of nickel is ~3000 cm$^2$ per cm$^2$ of the anode cross sectional area. To completely cover the surface with an adsorption layer ($\sqrt{3}\times\sqrt{3}$) rotated 30° (1/3 monolayer), assuming $10^{15}$ surface sites cm$^{-2}$, approximately $7\times10^{-7}$ mol Sb cm$^{-2}$ would be required. With a fuel gas flow rate of ~1 cm$^3$ gas cm$^{-2}$ cell area s$^{-1}$ used in present tests, corresponding to a typical fuel utilization of 10%, and an Sb concentration in coal gas of 1 ppm, available surface sites should be saturated within ~2 h, which is in good agreement with experimental observations. For a large SOFC stack operating at a fuel utilization of 90% and a Sb concentration of 0.07 ppm consistent with the expected average, available surface sites are expected to be saturated within 100–200 h. These losses in performance due to adsorption layer formation are very small, and probably can be ignored.

Later stage degradation due to the formation of binary Ni–Sb phases imposes more strict requirements. These reaction products can coalesce to form large grains on the surface of the anode and within the anode support, are the most visible of degradation processes. It is straightforward to estimate the time for conversion of Ni in the anode to NiSb, the product observed most extensively.

Assuming an Sb concentration in coal gas of 0.07 ppm (expected average for U.S. coals, but recognizing that some coal deposites contain considerably higher Sb concentrations than the average), an anode thickness of 500 μm, a Ni/YSZ volume ratio of 40/60, a porosity fraction of 0.3, and 90% fuel utilization at a power output of 0.5 W cm$^{-2}$, approximately 1 million h would be required for full anode conversion. For anode-supported cells, failure often occurred well before antimony-containing bulk phase formation reached the active anode/electrolyte interface. Failure of these cells occurred abruptly, whereas there was little evidence of cell degradation prior to complete failure. The mode of failure clearly is related to loss of electrical connectivity within the anode support. Failure with as little as 10% of the anode converted to reaction products was observed in laboratory tests, which corresponds to an estimated lifetime of 100,000 h. Further, as was shown in Fig. 12, Sb maybe captured preferentially at the fuel inlet of the stack, so damage could be localized within a small portion of the stack.

For electrolyte-supported cells, degradation appears to be diffusion controlled. When resistances given in Fig. 6b for the electrolyte supported cells were re-plotted as a function of square root time (not shown here), a linear fit was observed, suggesting a diffusion-controlled process for both ohmic and electrodic resistance increases that could be the Ni–Sb coalescence. While such behavior is of importance in relatively short laboratory tests performed at high Sb concentrations, the kinetics of coalescence in long term stack tests at low Sb concentrations is not expected to control the rate of degradation.

## 5. Conclusions

Tests were performed with both anode-supported and electrolyte-supported button cells in synthetic coal gas containing varying concentrations of Sb. Sb strongly interacted with nickel to form solid solution and a series of nickel antimonide phases $Ni_3Sb$, $Ni_5Sb_2$, NiSb for antimony concentrations ranging from 0.5 to 9 ppm. Both cell types quickly responded to the presence of Sb and a small voltage drop was attributed to the formation of a surface adsorption layer at the active interface similar to that of sulfur. Ohmic increases because of the Ni–Sb agglomeration were responsible for the irreversible long term degradation. In addition, tests with Ni/YSZ coupons were performed in both flow-through and flow-by configurations to provide information on relative uptake kinetics. These coupon tests demonstrated that Ni and Sb react rapidly in coal gas, and suggest that most Sb would be captured near the fuel inlet.

## Acknowledgements

The authors would like to acknowledge the help of G.W. Coffey and D. Conner for designing and fabricating the antimony holder, C.N. Cramer and J. Bonnett for cell fabricating, C. Chamberlin for SEM samples polishing. Support for this work was provided by the U.S. Department of Energy, Office of Fossil Energy, National Energy Technology Laboratory through the SECA Coal-Based Systems Core Research Program. Pacific Northwest National Laboratory is operated for the US Department of Energy by Battelle under Contract AC06-76RLO 1830.

## References

[1] T. Kivisaari, P. Bjornbom, C. Sylwan, B. Jacquinot, D. Jansen, A. de Groot, Chem. Eng. J. 100 (2004) 167–180.
[2] Y. Matsuzaki, I. Yasuda, Solid State Ionics 132 (2000) 261–269.
[3] S. Mukerjee, K. Haltiner, R. Kerr, L. Chick, V. Sprenkle, K. Meinhardt, C. Lu, J.Y. Kim, K.S. Weil, ECS Trans. 7 (2007) 59–65.
[4] K. Sasaki, K. Susuki, A. Iyoshi, M. Uchimura, N. Imamura, H. Kusaba, Y. Teraoka, H. Fuchino, K. Tsujimoto, Y. Uchida, N. Jingo, J. Electrochem. Soc. 153 (2006) A2023–A2029.
[5] O.A. Marina, C.A. Coyle, E.C. Thomsen, D.J. Edwards, G.W. Coffey, L.R. Pederson, Solid State Ionics 181 (2010) 430–440.
[6] C.A. Coyle, O.A. Marina, E.C. Thomsen, D.J. Edwards, C.N. Cramer, G.W. Coffey, L.R. Pederson, J. Power Sources 193 (2009) 730–738.
[7] C. Xu, M. Gong, J.W. Zondlo, X.B. Liu, H.O. Finklea, J. Power Sources 195 (2010) 2149–2158.
[8] D.J. Swaine, Trace Elements in Coal, Butterworths, London, 1990.
[9] R.B. Finkelman, in: M.H. Engel, S.A. Macko (Eds.), Organic Geochemistry, Plenum Press, New York, 1993.
[10] A. Martinez, K. Gerdes, R. Gemmen, J. Poston, J. Power Sources 195 (2010) 5206–5212.
[11] C.C. Qi, G.J. Liu, C.L. Chou, L.Q. Zheng, Sci. Total Environ. 389 (2008) 225–234.
[12] V.V. Seredin, Lithol. Miner. Resour. 38 (2003) 154–161.
[13] A.I. Karayigit, D.A. Spears, C.A. Booth, Int. J. Coal Geol. 44 (2000) 1–17.
[14] S.F. Dai, R.S. Zeng, Y.Z. Sun, Int. J. Coal Geol. 66 (2006) 217–226.
[15] J.J. Helble, W. Mojtahedi, J. Lyyranen, J. Jokiniemi, E. Kauppinen, Fuel 75 (1996) 931–939.
[16] R.H. Nielsen, P.K. Doolin, Stud. Surf. Sci. Catal. 76 (1993) 339–384.
[17] E.A. Karakhanov, N.F. Kovaliova, S.V. Lysenko, Vestn. Mosk. Univ., Seriya 2 Khimiya 39 (1998) 418–421.
[18] A. Corma, M.S. Grande, M. Iglesias, C. Delpino, R.M. Rojas, Appl. Catal. A: Gen. 85 (1992) 61–71.
[19] M.J. Dreiling, A.M. Schaffer, J. Catal. 56 (1979) 130–133.
[20] A. Krupski, S. Mroz, Surf. Rev. Lett. 10 (2003) 65–72.
[21] G.D. Parks, Appl. Surf. Sci. 5 (1980) 92–97.
[22] M.R. Goldwasser, D. Rojas, J. Goldwasser, J. Catal. 135 (1992) 596–608.
[23] J.P. Trembly, R.S. Gemmen, D.J. Bayless, J. Power Sources 163 (2007) 986–996.
[24] J.E. Bao, G.N. Krishnana, P. Jayaweeraa, J. Perez-Marianoa, A. Sanjurjoa, J. Power Sources 193 (2009) 607–616.
[25] K.D. Meinhardt, J.D. Vienna, T.R. Armstrong, L.R. Pederson, US patents 6,532,769 (2003) and 6,430,966 (2002).
[26] A. Roine, 6.12 ed., Outokumpu Research Oy, Pori, Finland.
[27] O.A. Marina, C.A. Coyle, M.H. Engelhard, L.R. Pederson, J. Electrochem. Soc. 158. (4) (2011), doi:10.1149/1.3552357.
[28] O.A. Marina, L.R. Pederson, C.A. Coyle, D.J. Edwards, Y.-S. Chou, C.N. Cramer, J. Power Sources 196 (2011) 636–643.
[29] H. Okamoto, J. Phase Equilib. Diffus. 30 (2009) 301–302.
[30] Z.M. Cao, Y. Takaku, I. Ohnuma, R. Kainuma, H.M. Zhu, K. Ishida, Rare Metals 27 (2008) 384–392.
[31] Y.B. Zhang, C.R. Li, Z.M. Du, C.P. Guo, Calphad-Comput. Coupling Phase Diag. Thermochem. 32 (2008) 378–388.
[32] T.J. Heames, D.A. Williams, N.E. Bixier, A.J. Grimley, C.J. Wheatley, N.A. Johns, P. Domagala, L.W. Dickson, C.A. Alexander, L. Osborne-Lee, S. Zawadzki, J. Rest, A. Mason, R.Y. Lee, NUREG/CR-5545 SADN90-0756 Rev.1, Sandia National Laboratories, 1992.
[33] Thermodynamic Properties of Compounds, SbO to SO2, Springer Materials – The Landolt-Börnstein Database, http://dx.doi.org/10.1007/10688868.14.
[34] O.A. Marina, L.R. Pederson, C.A. Coyle, E.C. Thomsen, D.J. Edwards, J. Electrochem. Soc. 158 (2011) B36–B43.
[35] H. Kishimoto, T. Horita, K. Yamaji, M.E. Brito, Y.P. Xiong, H. Yokokawa, J. Electrochem. Soc. 157 (2010) B802–B813.
[36] S. Katsuyama, M. Watanabe, M. Kuroki, T. Maehata, M. Ito, J. Appl. Phys. 93 (2003) 2758–2764.
[37] W. Liu, X. Sun, L.R. Pederson, O.A. Marina, M.A. Khaleel, J. Power Sources 195 (2010) 7140–7145.